Relationship Between the Crystallization Behavior and the Warpage of Film-Insert-Molded Parts

Jin Young Kim,[1] Seong Yun Kim,[2] Young Seok Song,[3] Jae Ryoun Youn[2]

[1]*Petrochemicals and Polymers R&D, LG Chem, Limited, Moonji-Dong, Yuseong-Gu, Daejeon 305-380, Korea*
[2]*Research Institute of Advanced Materials, Department of Materials Science and Engineering, Seoul National University, Sillim-Dong, Gwanak-Gu, Seoul 151-742, Korea*
[3]*Fiber System Engineering, Dankook University, Jukjeon-Dong, Suji-Gu, Yongin-Si, Gyeonggi-Do 448-701, Korea*

Received 18 May 2010; accepted 20 July 2010
DOI 10.1002/app.33076
Published online 30 November 2010 in Wiley Online Library (wileyonlinelibrary.com).

ABSTRACT: The dimensional variation of an injection-molded, semicrystalline polymer part is larger than the variation of an amorphous polymer part because the shrinkage of a crystalline polymer is generally greater than the shrinkage of an amorphous one. We investigated the warpage of film-insert-molded (FIM) specimens to determine the effect of the crystallization behavior on the deformation of FIM parts. More perfect crystalline structures and higher crystallinity developed in the core region of the FIM specimens versus other regions. Relatively imperfect crystalline structures and low crystallinity developed in the adjacent regions of the inserted films, whereas a thin, amorphous skin layer developed in the adjacent regions of the metallic mold wall. The crystallizable substrate in the FIM specimens caused very large warpage because nonuniform shrinkage occurred in the thickness direction of the specimens. Therefore, the warpage of an experimentally prepared FIM poly(butylene terephthalate) specimen was greater than that predicted numerically because of its complex crystallization behavior. © 2010 Wiley Periodicals, Inc. J Appl Polym Sci 120: 1539–1546, 2011

Key words: crystallization; injection molding; simulations; stress

INTRODUCTION

Injection molding is one of the most productive polymer processing methods because a wide variety of products with large and complex geometries or micropatterns and nanopatterns can be manufactured with precision. Film-insert molding is an efficient processing method for improving the surface quality of injection-molded products. Film-insert molding generally consists of three steps. First, an insert film that has been preformed to fit the cavity of a mold is attached to one of the mold walls. Second, a hot polymer melt is injected into the cavity. Third, the molded product is cooled and ejected. During film-insert molding, the surface of the inserted film is slightly melted by the injected hot resin, and good adhesion between the inserted film and the injected substrate is generated. Therefore, film-insert molding is a highly advanced molding method that does not involve postprocessing of surface treatments such as heat-induced labeling and screen printing. However, a nonuniform temperature distribution develops in the thickness direction during film-insert molding because the two polymers used as the insert film and the substrate resin have different thermal characteristics. As a result, nonuniform shrinkage of the ejected product is caused by the nonuniform temperature distribution, and warpage occurs because of the nonuniform shrinkage.

There have been many studies of the warpage of film-insert-molded (FIM) parts. Kim and coworkers[1,2] carried out a numerical analysis of film-insert molding and reported a warpage-reversal phenomenon in FIM specimens. An unannealed film-insert specimen was bent in such a way that the film side protruded after ejection and became concave after annealing of the entire FIM specimen. The warpage-reversal phenomenon was induced by the combined effects of thermal shrinkage of the inserted film and relaxation of residual stresses in the FIM specimen during annealing. More studies were performed to understand the warpage of FIM parts with respect to injection-molding parameters. Kim et al.[3] examined the effects of the mold wall temperature and packing pressure on the warpage of FIM parts. Baek et al.[4] studied the effects of the injection speed, melt temperature, and packing time on warpage. They also observed that the warpage of FIM specimens was proportional to the shrinkage of the injected substrate, which was affected by injection-molding conditions such as the injection speed,

Correspondence to: J. R. Youn (jaeryoun@snu.ac.kr).
Contract grant sponsor: Basic Science Research Program (through the National Research Foundation of Korea, which is funded by the Korean Ministry of Education, Science, and Technology); contract grant number: R11-2005-065.

packing time, and melt temperature. Oh et al.[5] studied the residual stress distribution, bending moment, and warpage of FIM specimens. Although injection-molding conditions for the film-insert molding of tensile specimens have been optimized by the Taguchi method, producing a perfectly flat specimen still remains as a challenge.[6]

Polymer materials are classified into two types: amorphous and semicrystalline. Because crystallization is a volumetric shrinkage behavior, the shrinkage of a crystalline polymer is generally greater than the shrinkage of an amorphous polymer. Hence, the dimensional variation of an injection-molded, semicrystalline polymer part is greater than that of an injection-molded, amorphous polymer part. An amorphous polycarbonate (PC)/acrylonitrile butadiene styrene (ABS) resin known to have low shrinkage was used in previous studies of the warpage of FIM specimens, as mentioned previously. If the warpage of an FIM specimen is proportional to the shrinkage of the injected substrate, as Baek et al.[4] reported, the warpage of FIM semicrystalline polymer parts and the effects of the crystallization behavior on the warpage of FIM specimens should be studied further because they have hardly been reported thus far. In this study, the warpage of FIM specimens made of a semicrystalline substrate was investigated to clarify the relationship between the warpage of the FIM specimens and the shrinkage of the injected substrate and then to examine the effect of the crystallization behavior on the warpage of the FIM specimens.

EXPERIMENTAL

Materials

A PC/ABS polymer blend (HP-1000X, Cheil Industries, Inc., Uiwang, Korea) and poly(butylene terephthalate) (PBT; Lupox GP-2000, LG Chem, Ltd., Daejeon, Korea) were used as the amorphous and semicrystalline substrates for film-insert molding. The densities of PC/ABS and PBT were 1.15 and 1.42 g/cm^3, respectively, according to ASTM D 792, and the mold shrinkage was 0.5–0.7% and 1.2–2.0%, respectively, according to ASTM D 955. The film employed for the experiment had a laminated structure consisting of ABS and poly(methyl methacrylate) (PMMA) layers. The PMMA thickness was 0.05 mm, and the thickness of the ABS layer was 0.45 mm according to the manufacturer (Nissha Printing Co., Ltd., Kyoto, Japan).

Film-insert molding

The PC/ABS blend and the PBT resin were dried at 80 and 90°C, respectively, in a vacuum oven for 4 h before injection molding to minimize the effect of moisture. The film was attached to the top and fixed side of the mold walls before the injection of the materials. The polymer resins were injected into a typical dog-bone-shaped cavity at 250°C with an injection-molding machine (Engel, Nürnberg, Germany). The maximum clamping force and screw diameter of the machine were 120 ton and 28 mm, respectively. Its maximum pressure and injection speed were 240 MPa and 600 mm/s, respectively. Injection molding was carried out with runners, two end gates, and cooling channels. Important molding conditions were as follows: a mold temperature of 60°C, an injection speed of 40 mm/s, a packing pressure of 8 MPa, and a packing time of 20 s.

Characterization

We prepared the specimens by slicing the molded sample to a thickness of 10 μm at −30°C with a cryotome (HM 505 E, Microm, Walldorf, Germany) to observe the cross section parallel to the melt flow direction. A Fourier transform infrared (FTIR) imaging system (FT/IR-6200, IMV-4000, Jasco, Tokyo, Japan) was used to determine the distribution of amorphous domains in the FIM specimens along the thickness direction (top, core, and bottom regions). Its resolution was set to 4 cm^{-1}, the wave-number scanning range was 4000–750 cm^{-1}, and the number of scans was 150. The intensity was calculated with the absorbance ratio of the amorphous band (1578 cm^{-1}) to the crystal band (1473 cm^{-1}).[7] Wide-angle X-ray diffraction (WAXD) profiles of the PBT specimens in the thickness direction were measured with an X-ray diffractometer (M18XHF-SRA, MAC Science Co., Yokohama, Japan) and Cu Kα X-rays (wavelength = 0.1542 nm). The diffraction intensity was recorded in the continuous scanning mode at the rate of 0.02°/s over the range of $10° < 2\theta < 40°$ (θ is the Bragg angle). The crystallite size of the specimen (L_{hkl}) was calculated with Scherrer's equation.[8–10]

$$L_{hkl} = \frac{K\lambda}{\beta \cos\theta} \quad (1)$$

where β is the half-width of the reflection peak, K is a correction factor (0.9), and λ is the wavelength of the X-ray beam used. The number of repeat units per crystal (N) in the specimen was calculated with the relation L_{hkl}/d, where d is the interplanar spacing. The thermal properties of the FIM PBT specimens were measured by differential scanning calorimetry (DSC; DSC-Q1000, TA Instrument, Crawley, UK). DSC specimens were also sampled from the same region used for the FTIR image specimens via slicing to a 20-μm thickness with the

cryotome at −30°C. The samples were heated from 25 to 250°C at a heating rate of 10°C/min under a nitrogen atmosphere. The crystallinity (X_c) of each sample was calculated with the heat of fusion:[9,11]

$$X_c(\%) = \frac{\Delta H_m}{\Delta H_m^o} \times 100 \tag{2}$$

where ΔH_m is the heat of fusion of PBT and ΔH_m^o is the heat of fusion of perfectly crystalline PBT (142 J/g).[12]

NUMERICAL SIMULATION

Flow analysis

The governing equations for the flow analysis in the mold cavity are the conservation of mass, conservation of momentum, and conservation of energy equations:[13,14]

$$\frac{D\rho}{Dt} + \rho(\nabla \cdot v) = 0 \tag{3}$$

$$\rho\frac{Dv}{Dt} = -\nabla P + \nabla \cdot \tau + \rho g \tag{4}$$

$$\rho C_p \frac{DT}{Dt} = \beta T \frac{DP}{Dt} + \eta\dot{\gamma}^2 + \nabla \cdot q \tag{5}$$

where ρ is the density, v is the velocity vector, P is the pressure, τ is the viscous stress tensor, g is the gravity/body-force vector, C_p is the specific heat at a constant pressure, β is the expansivity, η is the generalized Newtonian viscosity, q is the heat flux, t is the time, and T is the temperature. $\dot{\gamma}$ is the shear rate:

$$\dot{\gamma} = \sqrt{\left(\frac{\partial u}{\partial z}\right)^2 + \left(\frac{\partial v}{\partial z}\right)^2} \tag{6}$$

where u and v are the velocity components in the x and y directions, respectively. The flow front in the cavity is tracked with a fluid concentration (F) equation:

$$\frac{DF}{Dt} = 0 \tag{7}$$

Because inserts are treated as rigid bodies with no deformation or displacement, mass and momentum conservation in the inserted films is ignored. However, heat exchange between the inserted film and mold or polymer melt needs to be evaluated. Hence, the energy balance must be taken into account in the process. The only equation relevant to an inserted film is the conservation of energy. Under the assumption that an insert is a rigid body, the conservation of energy equation for the cavity given in eq. (5) can be simplified for inserts as follows:[13,14]

$$\rho C_p \frac{\partial T}{\partial t} = \nabla \cdot q \tag{8}$$

Residual stress calculation

Residual stress models are generalizations of Hooke's law, which for an elastic solid has the following form:

$$\sigma_{ij} = c^e_{ijkl}\varepsilon_{kl} \tag{9}$$

where σ_{ij} and ε_{kl} are the stress and total strain tensors, respectively, and c^e_{ijkl} is the tensor of elastic constants. The strain tensor (ε_{ij}) is determined by differentiation of the components of the displacement ($\overline{u}$) and is defined as follows:

$$\varepsilon_{ij} = \tfrac{1}{2}\left(u_{i,j} + u_{j,i}\right) \tag{10}$$

where $u_{i,j}$ and $u_{j,i}$ are differentiation of the components of the displacement.

Residual stress models are frequently formulated with a viscoelastic constitutive relationship.[15,16] A general linear, anisotropic, thermoviscoelastic constitutive relationship can be written as follows:

$$\sigma_{ij} = \int_0^t c_{ijkl}(\xi(t) - \xi(t'))\left(\frac{\partial \varepsilon_{kl}}{\partial t'} - \alpha_{kl}(\xi(t) - \xi(t'))\frac{\partial T}{\partial t'}\right)dt' \tag{11}$$

where c_{ijkl} is the viscoelastic relaxation modulus and α_{kl} is the tensor of coefficients of expansion, t' is a dummy variable. $\xi(t)$ is a pseudo-timescale defined as follows:

$$\xi(t) = \int_0^t \frac{1}{a_T}dt'$$

where a_T is the time–temperature shift factor accounting for the effect of the temperature on the material response. However, we are faced with an intricate problem when we use eq. (11) for nonisothermal systems. First, eq. (11) assumes that a material is thermorheologically simple. Unfortunately, it is not always possible to obtain material data for relaxation functions satisfying the assumption of thermorheological simplicity because a large number of real materials are actually thermorheologically complex. Second, the relaxation functions used in eq. (11) may depend on the internal structures, which themselves are in turn affected by processing conditions; this is particularly true for those systems involving semicrystalline

TABLE I
Constants of the Hybrid Residual Stress Equation for the Materials

	A_1	A_2	A_3	A_4	A_5	A_6
PC/ABS	0.377360	−0.139408	0.004557	0.456699	−0.177767	0.005319
PBT	0.462313	−0.293653	0.010463	1.728920	0.088405	−0.009747

materials and phase changes. The exact relationship between the internal structures and the relaxation functions is largely unknown (either theoretically or experimentally). Because of the aforementioned complexity related to the viscoelastic data, it is common to further approximate the problem with a viscoelastic calculation in which the material is assumed to sustain no stress above a certain temperature known as the transition temperature (T_t). Below T_t, the material is assumed to be elastic and able to sustain stress. Under this assumption, we have the following:

$$\sigma_{ij} = \int_0^t c^e_{ijkl}(t)\left(\frac{\partial \varepsilon_{kl}}{\partial t'} - \alpha_{kl}(t)\frac{\partial T}{\partial t'}\right)dt' \tag{12}$$

The hybrid model uses measured shrinkage data to improve the prediction of shrinkage and warpage from a theoretical model such as eq. (12). It may be used for filled and unfilled materials and appears to perform well for polymer blends. For unfilled materials, the model has the following form:

$$\begin{aligned} \sigma_e^{\parallel} &= A_1\sigma_P + A_2\tau + A_3 \\ \sigma_e^{\perp} &= A_4\sigma_P + A_5\tau + A_6 \end{aligned} \tag{13}$$

where $\sigma_e^{\parallel}$ and $\sigma_e^{\perp}$ are the corrected principal stresses in the directions parallel and transverse to flow, respectively; σ_P is the predicted residual stress; A_i ($i = 1 \ldots 6$) is a constant to be determined; and τ is a measure of orientation in the material. The A_i values ($i = 1 \ldots 6$) of the used polymer materials are listed in Table I. The predicted stresses are considered isotropic. Consequently, the thermomechanical properties used in their determination may also be isotropic. This simplifies the required material data significantly. Although this simplification ignores the observed isotropy in measured samples, the model introduces orthotropy into the corrected residual stresses. For unfilled amorphous materials, the observed shrinkage anisotropy, parallel and transverse to the flow, is usually small. However, even small variations can significantly affect the warpage of parts with low torsional stiffness. For these materials, the degree of anisotropy may be related to the orientation of molecules in the material. Semicrystalline polymers develop a complex layered morphology that governs the thermomechanical properties of the materials and influences shrinkage anisotropy.[17] Although general relationships have not yet been developed, it does appear that the resulting morphology is related to the molecular orientation of the materials before solidification. In this study, we have assumed that the orientation state can be measured as a function of the cooling rate (dT/dt), the second invariant of the deformation rate tensor (Π_D), and the relaxation time (λ):

$$\tau = \tau\left(II_D, \frac{dT}{dt}, \lambda\right) \tag{14}$$

Material properties

The non-Newtonian viscosity can be represented by the modified Cross model:[18,19]

$$\eta(T, \dot{\gamma}, p) = \frac{\eta_0(T, p)}{1 + \left(\eta_0(T, p)\dot{\gamma}/\tau^*\right)^{1-n}} \tag{15}$$

where η is the viscosity, η_0 is the zero-shear-rate viscosity, τ^* is the shear stress at the transition between Newtonian and power-law behavior, and n is the power-law index. η_0 can be represented as a function of temperature by the Williams–Landel–Ferry (WLF) equation:

$$\eta_0(T, p) = D_1 \exp\left(-\frac{A_1(T - T^*(p))}{\tilde{A}_2 + D_3 p + (T - T^*(p))}\right) \tag{16}$$

where p is pressure, $T^*(p)$ is pressure dependent temperature, $\tilde{A}_2$, D_1, D_2, D_3 are data-fitted coefficients; $T^*(p)$ is equal to $D_2 + D_3 p$. There are seven constants

TABLE II
Constants of the Modified Cross Model with the WLF Equation for the Materials

	n	τ^* (Pa)	D_1 (Pa s)	D_2 (K)	D_3 (K/Pa)	A_1	$\tilde{A}_2$ (K)
PC/ABS	0.2917	321,451	3.1229×10^8	417.15	0	18.442	51.6
PBT	0.6540	592,000	1.0000×10^{12}	350.99	0	28.946	51.6

TABLE III
Constants of the Modified Tait Equation for the Materials

Coefficient	PC/ABS	PBT	Unit
b_5	401.15	494.15	K
b_6	3.298×10^{-7}	1.665×10^{-7}	K/Pa
b_{1m}	0.0008990	0.0009041	m^3/kg
b_{2m}	6.109×10^{-7}	8.031×10^{-7}	m^3/kg K
b_{3m}	1.7093×10^{8}	$9.5240e \times 10^{7}$	Pa
b_{4m}	0.004330	0.003702	1/K
b_{1s}	0.0008990	0.0008519	m^3/kg
b_{2s}	2.978×10^{-7}	4.588×10^{-7}	m^3/kg K
b_{3s}	2.37547×10^{8}	1.19200×10^{8}	Pa
b_{4s}	0.003361	0.005373	1/K
b_7	0	4.633×10^{-5}	m^3/kg
b_8	0	0.1436	1/K
b_9	0	2.371×10^{-8}	1/Pa

in eqs. (15) and (16), and the values for the used polymer materials are listed in Table II. The modified Tait equation describes the pressure–volume–temperature relationship of polymer materials.[14]

$$V(T,P) = V_0(T)\left[1 - C\ln\left(1 + \frac{P}{B(T)}\right)\right] + V_t(T,P) \tag{17}$$

where $V(T,P)$ is the specific volume at temperature T and pressure P, V_0 is the specific volume at a gauge pressure of 0, C is a constant (0.0894), and B accounts for the pressure sensitivity of the material [it is defined in eq. (19)]. The upper temperature region ($T > T_t$) can be described with the following equations:

$$V_0 = b_{1m} + b_{2m}(T - b_5) \tag{18}$$

$$B(T) = b_{3m}\exp[-b_{4m}(T - b_5)] \tag{19}$$

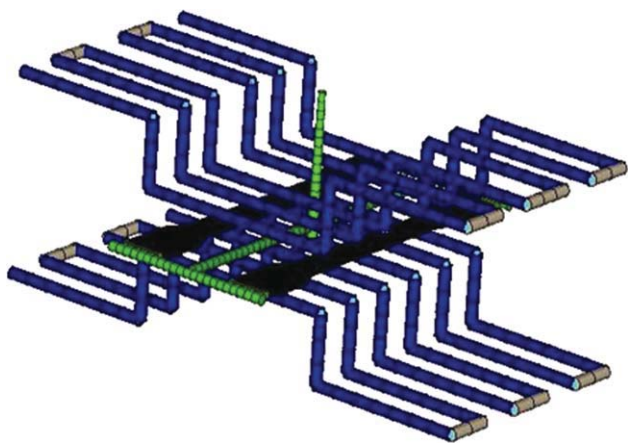

Figure 1 Finite element model of the runners, gates, cooling channels, and dog-bone-shaped part. [Color figure can be viewed in the online issue, which is available at wileyonlinelibrary.com.]

TABLE IV
Material Properties of the Polymer Resin and Film Used for the Numerical Simulation

	PC/ABS	PBT	Film
Elastic modulus (MPa)	2510	2600	2240
Poisson's ratio	0.402	0.437	0.392
Melt density (kg/m^3)	1027.2	1078.3	943.9
Solid density (kg/m^3)	1151.6	1312.4	1054.1
Thermal expansion coefficient (K^{-1})	6.93×10^{-5}	7.75×10^{-5}	8.00×10^{-5}
Thermal conductivity (W/m °C)	0.195 (at 79°C)	0.190 (at 250°C)	0.116 (at 75°C)
Specific heat (J/kg °C)	2290 (at 203°C)	2262 (at 250°C)	2202 (at 200°C)

$$V_t(T,P) = 0 \tag{20}$$

where b_{1m}, b_{2m}, b_{3m}, b_{4m}, and b_5 (which represents T_t at a gauge pressure of 0) are data-fitted coefficients. The lower temperature region ($T < T_t$) can be described as follows:

$$V_0 = b_{1s} + b_{2s}(T - b_5) \tag{21}$$

$$B(T) = b_{3s}\exp[-b_{4s}(T - b_5)] \tag{22}$$

$$V_t(T,P) = b_7\exp((b_8(T - b_5)) - (b_9P)) \tag{23}$$

where b_{1s}, b_{2s}, b_{3s}, b_{4s}, b_5, b_7, b_8, and b_9 are data-fitted coefficients. The dependence of T_t on pressure can be described by the following equation:

$$T_t(P) = b_5 + b_6P \tag{24}$$

where b_5 and b_6 are data-fitted coefficients. The data-fitted coefficients of the used polymer materials are listed in Table III.

A finite element model of runners, gates, cooling channels, and a dog-bone-shaped part is shown in Figure 1. We treated the laminated PMMA/ABS film as a homogeneous film by neglecting the PMMA layer because the thickness of the PMMA layer was relatively small. The properties of the ABS resin (Techno ABS 545, Techno Polymer, Detroit, MI) were used as the properties of the film. The physical properties of the polymer materials are summarized in Table IV, and the processing conditions for the numerical analysis were the same as the experimental conditions. We modeled the ejection step numerically by solving the elasticity after fixed boundary conditions were removed suddenly.

RESULTS AND DISCUSSION

The crystallization of semicrystalline polymers generally causes substantial shrinkage, which affects the dimensional accuracy of injection-molded parts. The warpage of FIM specimens prepared with an

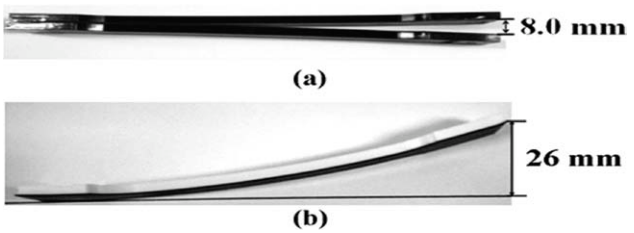

Figure 2 Warpage of the FIM specimens: (a) the amorphous PC/ABS blend substrate and (b) the semicrystalline PBT substrate.

amorphous PC/ABS blend and semicrystalline PBT is shown in Figure 2. Both specimens were bent in such a way that the film side was convex regardless of the crystalline behavior because the shrinkage of the solid film side was less than the shrinkage of the other side (where the polymer melt was solidified). The warpage of the PBT specimen was much greater than the warpage of the PC/ABS specimen because of the large shrinkage of the injected PBT resin that underwent crystallization. In a previous study,[4] the warpage of FIM specimens was proportional to the shrinkage of the injected substrate.

The numerically predicted warpage of the FIM specimens prepared with the amorphous PC/ABS substrate and the semicrystalline PBT substrate is shown in Figure 3. The numerical results presented in Figure 3(a,b) are consistent with the experimental ones shown in Figure 2(a,b), respectively. The numerical results for the FIM PC/ABS specimens agreed with the experimental results reported in previous studies.[2–4] In contrast, the predicted warpage of the FIM PBT specimen was relatively small in comparison with the experimental results because of the crystallization behavior of the PBT resin.

The distributions of amorphous domains in the FIM PBT specimens, which were observed with the FTIR imaging system, are shown in Figure 4. The high- and low-intensity regions correspond to areas of high and low amorphousness, respectively. The lowest and highest distributions of the amorphous domains were observed in the core and bottom regions. In comparison with the distribution in the core region, a slightly higher distribution of amorphous domains was detected in the top region because the slowest solidification occurred in the core region of the specimen, and heat transfer from the core region to the solid film was retarded by the inserted film, the thermal conductivity of which was

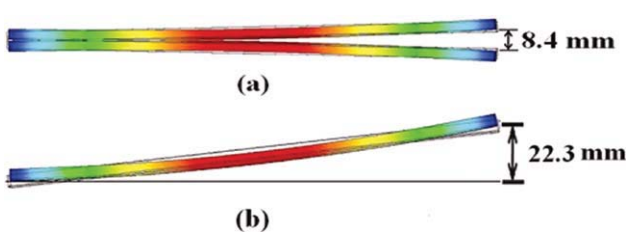

Figure 3 Predicted warpage of the FIM specimens: (a) the amorphous PC/ABS substrate and (b) the semicrystalline PBT substrate. [Color figure can be viewed in the online issue, which is available at wileyonlinelibrary.com]

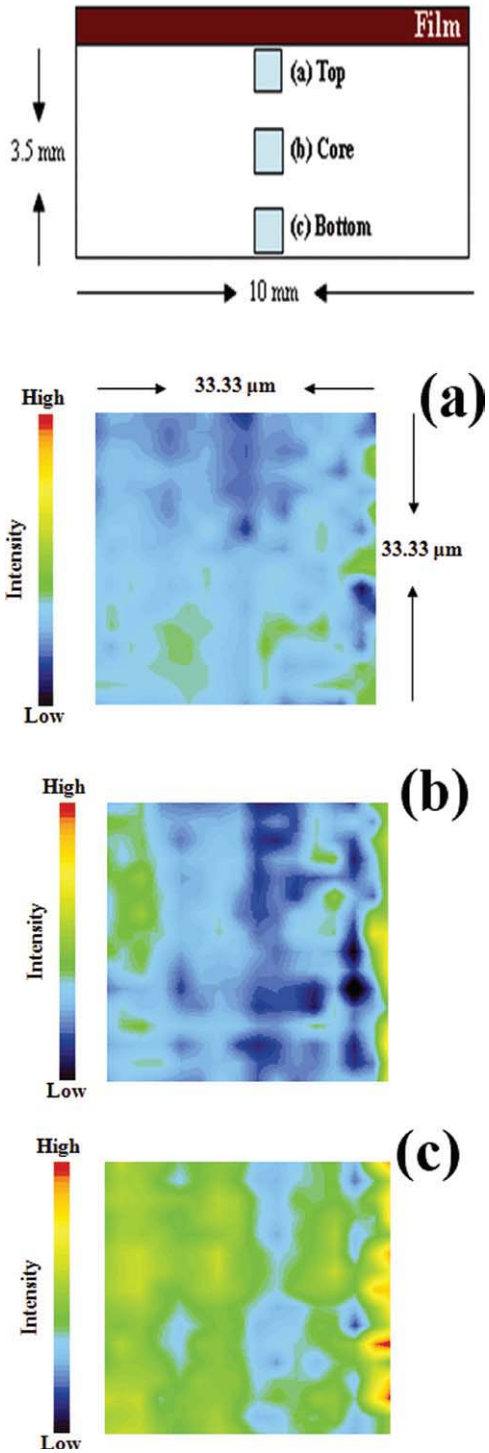

Figure 4 FTIR images depicting the distribution of amorphous domains in the FIM specimen: (a) top, (b) core, and (c) bottom regions. [Color figure can be viewed in the online issue, which is available at wileyonlinelibrary.com]

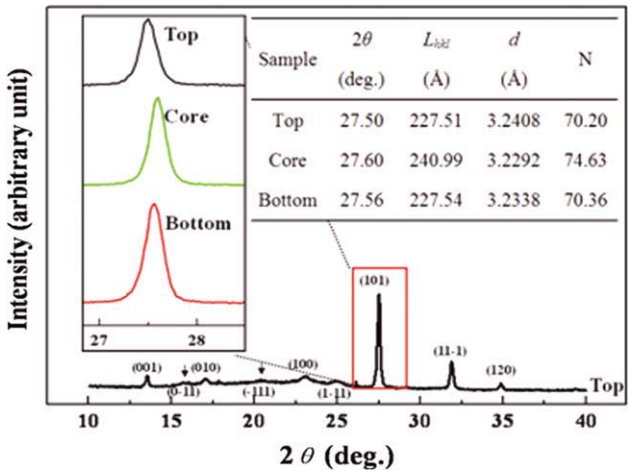

Figure 5 WAXD profiles of the FIM PBT specimen: top, core, and bottom regions. [Color figure can be viewed in the online issue, which is available at wileyonlinelibrary.com]

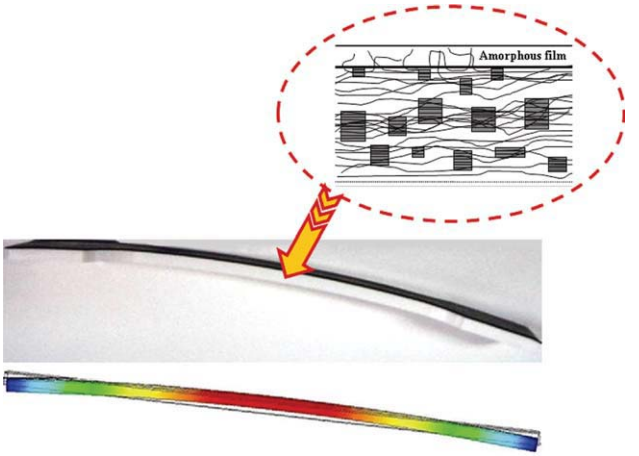

Figure 7 Numerical and experimental results for the warpage with a schematic diagram showing the crystalline structure in the FIM PBT specimen. [Color figure can be viewed in the online issue, which is available at wileyonlinelibrary.com]

much smaller than that of the metal mold. An amorphous skin layer developed in the bottom region because of the fast heat transfer between the injected polymer resin and metallic mold walls. On the other hand, a relatively imperfect crystalline skin layer developed in the top region because of the retarded heat transfer between the injected polymer resin and the film. Yamaguchi et al.[20] reported that the heat transfer was retarded in the FIM specimen, and an amorphous skin layer approximately 1 μm thick was generated between the injected PP resin and metal mold.[20]

WAXD profiles of the FIM specimen in the thickness direction are shown in Figure 5. Nine characteristic crystalline peaks were observed at 2θ values of 13.6, 15.7, 17, 20.3, 23.08, 24.85, 27.3, 31.98, and 34.86°, which corresponded to the (001), (0−11), (010), (−111), (100), (1−11), (101), (11−1), and (120) reflections, respectively.[12,21–25] The apparent crystallite size and the number of repeat units per crystal were calculated from the (101) reflection peak, the intensity of which was the highest in the top, core, and bottom regions. The results are summarized in the table inserted in Figure 5. The crystallite size and the number of repeat units per crystal were largest and smallest in the core and top regions, respectively. The crystallite size was slightly larger in the bottom region versus the top region. It is known that the number of repeat units per crystal is a good measure for evaluating the degree of perfection of crystals. Therefore, the WAXD results were due to the fact that the crystallite size was larger in the order of the core, bottom, and top regions. When we consider the results of the FTIR images, the WAXD results can be explained by the fact that X-rays applied in the direction of the bottom region penetrated the amorphous skin layer and were reflected to the inner crystalline structure above it.

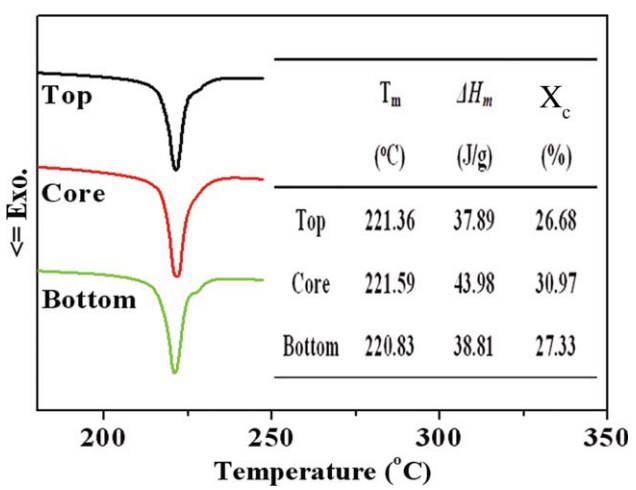

Figure 6 DSC curves of the FIM PBT specimen: top, core, and bottom regions (T_m = melting temperature). [Color figure can be viewed in the online issue, which is available at wileyonlinelibrary.com]

To characterize the crystallization behavior of the FIM specimens, their thermal behavior was studied with DSC, as shown in Figure 6. The crystallinity of the core region that was obtained from the DSC results was somewhat higher than that of the other regions, whereas those of the top and bottom regions were almost the same because the thickness of the amorphous skin layer of the bottom region was thin, and the crystallinity was affected slightly by the amorphous skin layer. The warpage of the FIM specimens was predicted numerically and was observed experimentally, as shown in Figure 7. A

schematic diagram has been inserted into the figure to show the crystalline structure in the FIM PBT specimen. The schematic diagram, showing the crystalline structure of the FIM PBT specimen, indicates that the most perfect and largest crystalline structure developed in the core region, and a small, imperfect crystalline structure developed in the top region. A thin, amorphous skin layer was generated in the very bottom region, and a relatively large and perfect crystalline structure developed in the region adjacent to the amorphous skin layer at the bottom. The interesting crystalline behavior of the FIM specimens induced much larger warpage of the FIM specimens with a crystallizable substrate because of the nonuniform shrinkage generated with respect to the center line of the specimens in the thickness direction.

CONCLUSIONS

The effects of the crystallization behavior on the warpage of FIM specimens were investigated. A perfect crystalline structure and higher crystallinity developed in the core region versus the other regions of FIM specimens. A relatively imperfect crystalline structure and low crystallinity developed in the adjacent region of an inserted film, and a thin, amorphous skin layer developed in the adjacent region of the metallic mold wall. The crystallization of the substrate in an FIM specimen caused large warpage because of the large and nonuniform shrinkage of the part in the thickness direction of the specimen. Although the pressure–volume–temperature relationship of the injected polymer resin was considered in the numerical simulation to predict the shrinkage of an injected specimen, the predicted warpage of an FIM specimen with a semicrystalline substrate was underestimated because of the complicated crystallization behavior of the substrate resin.

References

1. Kim, S. Y.; Oh, H. J.; Kim, S. H.; Kim, C. H.; Lee, S. H.; Youn, J. R. Polym Eng Sci 2008, 48, 1840.
2. Kim, S. Y.; Kim, S. H.; Oh, H. J.; Lee, S. H.; Baek, S. J.; Youn, J. R.; Lee, S. H.; Kim, S. W. J Appl Polym Sci 2009, 111, 642.
3. Kim, S. Y.; Lee, S. H.; Baek, S. J.; Youn, J. R. Macromol Mater Eng 2008, 293, 969.
4. Baek, S. J.; Kim, S. Y.; Lee, S. H.; Youn, J. R.; Lee, S. H. Fiber Polym 2008, 9, 747.
5. Oh, H. J.; Song, Y. S.; Lee, S. H.; Youn, J. R. Polym Eng Sci 2009, 49, 1389.
6. Kim, S. Y.; Lee, S. H.; Youn, J. R. Int Polym Process 2010, 2, 1.
7. Kalkar, A. K.; Siesler, H. W.; Pfeifer, F.; Wadekar, S. A. Polymer 2003, 44, 7251.
8. Alexander, L. E. X-Ray Diffraction Methods in Polymer Science; Wiley: New York, 1969.
9. Kim, S. Y.; Kim, J. Y.; Kim, S. H. Polym Int 2008, 57, 378.
10. Kim, S. Y.; Kim, S. H.; Lee, S. H.; Youn, J. R. Compos A 2009, 40, 607.
11. Kim, S. Y.; Kim, S. H.; Kim, J. Y.; Cho, H. H. J Appl Polym Sci 2007, 104, 205.
12. Vendramini, J.; Bas, C.; Merle, G.; Boissonnat, P.; Alberola, N. D. Polym Compos 2000, 21, 724.
13. Macosko, C. W. Rheology: Principles, Measurements, and Applications; Wiley-VCH: New York, 1994.
14. Kennedy, P. Flow Analysis Reference Manual; Moldflow: Kilsyth, Australia, 1993.
15. Baaijens, F. P. T. Rheol Acta 1991, 30, 284.
16. Rezayat, M.; Stafford, R. O. Polym Eng Sci 1991, 31, 393.
17. Zuidema, H. Ph.D. Thesis, Eindhoven University of Technology, 2000.
18. Zoetelief, W. F.; Douven, L. F. A.; Ingen Housz, A. J. Polym Eng Sci 1996, 36, 1886.
19. Hastenberg, C. H. V.; Wildervanck, P. C.; Leenen, A. J. H. Polym Eng Sci 1992, 32, 506.
20. Yamaguchi, S.; Leong, Y. W.; Tsujii, T.; Mizoguchi, M.; Ishiaku, U. S.; Hamada, H. J Appl Polym Sci 2005, 98, 294.
21. Font, J.; Muntasell, J.; Cesari, E. Mater Res Bull 1999, 34, 157.
22. Munehisa, Y.; Shinsuke, T.; Kazuhito, O.; Shin'ichi, T. J Polym Sci Part B: Polym Phys 2001, 39, 2005.
23. Sahoo, N. G.; Das, C. K.; Pandey, K. N.; Mathur, G. N. Mater Lett 2002, 56, 194.
24. Hsiao, B. S.; Wang, Z.; Yeh, F.; Gao, Y.; Sheth, K. C. Polymer 1999, 40, 3515.
25. Park, C. S.; Lee, K. J.; Kim, S. W.; Lee, Y. K.; Nam, J. D. J Appl Polym Sci 2002, 86, 478.